The Lyme Disease Pathogen *Borrelia burgdorferi* Infects Murine Bone and Induces Trabecular Bone Loss

Tian Tian Tang,[a] Lucia Zhang,[b,c] Anil Bansal,[a] Marc Grynpas,[c,d] Tara J. Moriarty[a,d]

Matrix Dynamics Group, Faculty of Dentistry, University of Toronto, Toronto, ON, Canada[a]; Department of Pharmacology and Toxicology, University of Toronto, Toronto, ON, Canada[b]; Lunenfeld-Tanenbaum Research Institute of Mount Sinai Hospital, Toronto, ON, Canada[c]; Department of Laboratory Medicine and Pathobiology, University of Toronto, Toronto, ON, Canada[d]

ABSTRACT Lyme disease is caused by members of the *Borrelia burgdorferi sensu lato* species complex. Arthritis is a well-known late-stage pathology of Lyme disease, but the effects of *B. burgdorferi* infection on bone at sites other than articular surfaces are largely unknown. In this study, we investigated whether *B. burgdorferi* infection affects bone health in mice. In mice inoculated with *B. burgdorferi* or vehicle (mock infection), we measured the presence of *B. burgdorferi* DNA in bones, bone mineral density (BMD), bone formation rates, biomechanical properties, cellular composition, and two- and three-dimensional features of bone microarchitecture. *B. burgdorferi* DNA was detected in bone. In the long bones, increasing *B. burgdorferi* DNA copy number correlated with reductions in areal and trabecular volumetric BMDs. Trabecular regions of femora exhibited significant, copy number-correlated microarchitectural disruption, but BMD, microarchitectural, and biomechanical properties of cortical bone were not affected. Bone loss in tibiae was not due to increased osteoclast numbers or bone-resorbing surface area, but it was associated with reduced osteoblast numbers, implying that bone loss in long bones was due to impaired bone building. Osteoid-producing and mineralization activities of existing osteoblasts were unaffected by infection. Therefore, deterioration of trabecular bone was not dependent on inhibition of osteoblast function but was more likely caused by blockade of osteoblastogenesis, reduced osteoblast survival, and/or induction of osteoblast death. Together, these data represent the first evidence that *B. burgdorferi* infection induces bone loss in mice and suggest that this phenotype results from inhibition of bone building rather than increased bone resorption.

KEYWORDS Borrelia burgdorferi, Lyme disease, bone, bone mineral density, histomorphometry, host-pathogen interactions, infectious disease, microcomputed tomography, mouse model, osteopenia

Lyme disease is the most common vector-borne disease in the Northern Hemisphere (1). Its causative agents are spirochetes from the *Borrelia burgdorferi sensu lato* species complex (2). These bacteria are not known to secrete conventional toxins and are therefore postulated to induce pathology primarily by triggering host inflammatory response (3). *B. burgdorferi* is transmitted to vertebrates during the blood meal of *Ixodes* spp. ticks and disseminates from the tick bite site to colonize a variety of host tissues. This can result in diverse clinical manifestations at various infection stages (4). In humans, erythema migrans (EM), a bull's-eye-shaped skin lesion, typically appears at the bite site 1 to 2 weeks postfeeding. If antibiotic treatment does not begin at this early infection stage, *B. burgdorferi* disseminates to more distant tissues, and late-stage manifestations such as Lyme arthritis, carditis, and neuroborreliosis can develop. Of
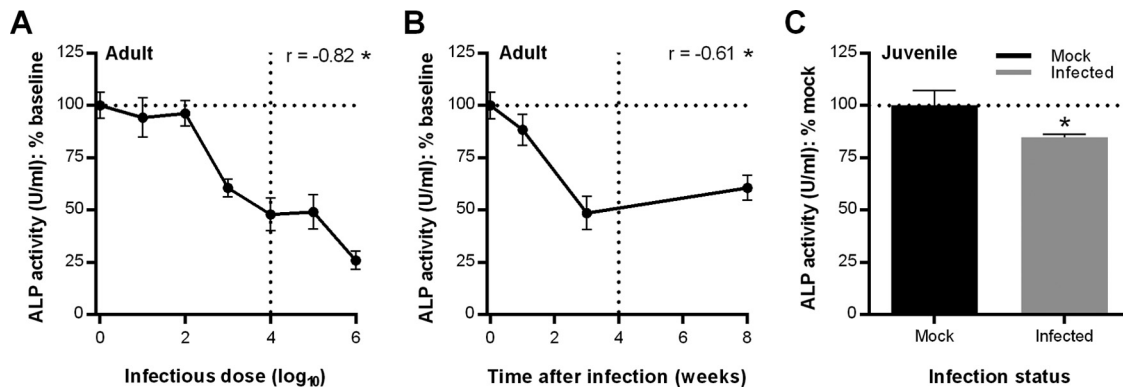
FIG 1 Effect of *B. burgdorferi* infection on ALP, a serum marker of bone formation. The mean ($\pm$ standard error of the mean) serum ALP activity is shown, after normalization to the mean baseline ALP activity immediately preceding infection (0 weeks) (A and B) or in mock-infected mice (C). Primary data are presented in Fig. S1 in the supplemental material. (A and B) Serum ALP activity in adult (16- to 17-week-old) male C3H/HeN mice infected for 3 weeks with 10^1 to 10^6 B31-derived GCB726 *B. burgdorferi* bacteria (A) or for 1, 3, and 8 weeks with 10^4 bacteria (B). $n = 5$ mice/group (A) or 10 mice/group (B). Statistics used were Pearson correlation analysis (r). *, $P < 0.05$ versus dose (A) or time (B). (C) Serum ALP activity in juvenile (3- to 4-week-old) male C3H/HeN mice infected for 4 weeks with 10^4 *B. burgdorferi* cells. Mock is the age-matched mice inoculated with vehicle alone. $n = 10$ mice/group. Statistical analysis used a two-tailed unpaired *t* test. *, $P < 0.05$ versus mock-infected controls.

these late-stage symptoms, Lyme arthritis is the most common in North America, affecting as many as 60% of untreated patients (5). The pathological effects of *B. burgdorferi* infection on bone tissue outside articular surfaces, however, have not been widely investigated.

Bone pathologies are observed in diseases associated with other spirochete bacteria, including syphilis and periodontitis (6, 7). Bone is central to physiological homeostasis of the whole body and to systemic responses to infection, injury, and a variety of stressors (8). Infections within bone, as well as induction of local and systemic inflammatory responses to infection at other sites, can be accompanied by significant bone loss (8, 9). *B. burgdorferi* has been detected by culture and PCR in bone and marrow of humans, dogs, and the mummy of a Copper Age man (10–13). Furthermore, migratory bone pain, bone erosion at articular surfaces, multifocal osteomyelitis, and other bone involvement have been reported in *B. burgdorferi*-infected rodents and humans (5, 12–21). In the course of other studies requiring collection of bone marrow, we have noticed that long bones from *B. burgdorferi*-infected mice occasionally appear to be more brittle than bones of mock-infected controls. This prompted us to examine whether *B. burgdorferi* induces structural and cellular pathology in murine bones.

RESULTS

***B. burgdorferi* infection reduces serum alkaline phosphatase activity, a biomarker of bone formation.** Alkaline phosphatase (ALP) catalyzes monoester hydrolysis and is involved in many physiological processes, including bone formation (22, 23). The liver and bone-building osteoblasts are two examples of numerous sources of ALP in the body (24). Unlike in humans, where serum ALP is derived primarily from the liver, in mice serum ALP consists mainly of tissue-nonspecific bone isotype ALP (bone TNAP) and therefore serves as a biomarker of bone formation (24, 25).

In 16-week-old adult male C3H/HeN mice infected with 10 to 10^6 B31-derived *B. burgdorferi* for 3 weeks, serum ALP activity declined with increasing infectious dose relative to ALP levels immediately before infection, especially for mice inoculated with $\geq 10^3$ bacteria (Fig. 1A). In mice infected with 10^4 *B. burgdorferi*, serum ALP activity declined with increasing infection duration, with the most prominent reduction in activity observed at 3 weeks postinoculation (Fig. 1B), when pathological outcomes of *B. burgdorferi* infection are typically most pronounced in C3H mice (26). Juvenile mice, which are typically more commonly used for Lyme disease studies (27), also displayed reduced serum ALP activity after 4 weeks of infection with 10^4 *B. burgdorferi* bacteria compared to mock-infected mice (Fig. 1C). The effect of *B. burgdorferi* infection on

FIG 2 Detection of *B. burgdorferi* DNA in bones. Quantitative real-time PCR measurement of copies of the *B. burgdorferi* *flaB* DNA sequence in distal tibial halves and L6 vertebrae from 12-week-old male C3H/HeN mice 4 weeks after inoculation with 10^4 *B. burgdorferi* cells or vehicle alone (mock). Shown are median and individual numbers of *flaB* copies per 1,000 copies of the mouse *nidogen* gene (*nido*) in each sample. $n = 14$ to 15 per group. Statistical analysis used a two-way analysis of variance with the Holm-Sidak posttest of log-transformed values. *, $P < 0.05$.

serum ALP activity was less prominent than in older mice, likely because bones in juvenile animals are still undergoing rapid bone formation and skeletal development (28). These data prompted us to investigate whether *B. burgdorferi* colonizes bone and/or affects bone health.

Bone colonization by *B. burgdorferi*. We examined *B. burgdorferi* colonization and infection effects on bone in 12-week-old adult male C3H/HeN mice. At this age, murine bone development stabilizes, and peak bone mineral density (BMD), trabecular volume, and cortical thickness are attained (28, 29). Mice were infected for 4 weeks with 1×10^4 B31-derived *B. burgdorferi* bacteria. Bone morphology, cellular composition, mineralization, growth rate, and biomechanical properties were investigated in long bones (tibiae, femora) and vertebrae, since long bones and vertebrae can exhibit different degrees of response to external stimuli. For example, rosiglitazone, a common antidiabetic drug, increases fracture risks in women in the limbs but not in vertebrae (30).

We first investigated whether *B. burgdorferi* could colonize murine bone. DNA was extracted from cleaned, crushed L6 vertebrae and distal halves of tibiae from which associated soft tissues and bone marrow had been removed (see Materials and Methods). Distal regions of tibiae were examined to ensure samples were collected as far from joints as possible, since joints are typically readily colonized by *B. burgdorferi*. It was more difficult to remove all surrounding soft tissues from vertebrae than from tibiae. Although we were confident that any bacterial DNA detected in tibiae likely originated from bone itself, we could not be certain that *B. burgdorferi* DNA detected in vertebrae was entirely bone derived. Total copies of a portion of the *B. burgdorferi* *flaB* gene and mouse *nidogen* DNA sequence were measured in each sample by quantitative real-time PCR (qPCR), and the *flaB* copy number/1,000 copies of *nidogen* was compared in different bones of mock-infected and infected mice (Fig. 2). *flaB* DNA copy number was significantly greater than background in mock-infected animals in the tibiae but not in vertebrae of infected mice (Fig. 2), indicating that tibiae were colonized more effectively. The *flaB:nidogen* copy number ratios in tibiae were similar to those previously reported in other tissues of *B. burgdorferi*-infected mice (31), implying that *B. burgdorferi* can colonize regions of long bones distal to articular surfaces as efficiently as other tissues.

***B. burgdorferi* infection induces osteopenia in the trabecular region of long bones.** To determine if *B. burgdorferi* bone colonization induced pathology, we measured areal and volumetric bone mineral density (aBMD and vBMD) in the left femora and L5 vertebrae from mock-infected and infected animals, using dual-energy X-ray absorptiometry (DXA) and microcomputed tomography (μCT). The effects of *B. burgdorferi* infection on trabecular and cortical bone were also compared using three-
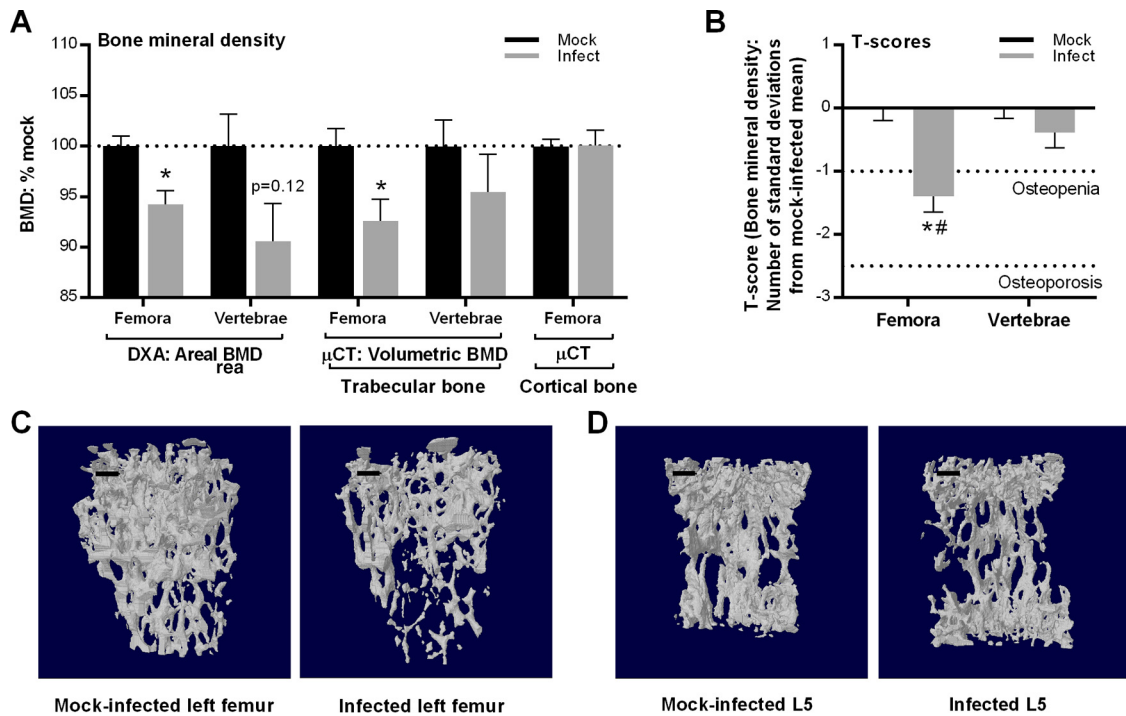
FIG 3 Effect of *B. burgdorferi* infection on bone mineral density. Areal and volumetric bone mineral densities were measured by DXA and μCT, respectively, in distal femoral metaphyses and L5 vertebrae from 12-week-old C3H/HeN male mice infected for 4 weeks with 10^4 *B. burgdorferi* cells or mock infected with vehicle alone. Values were normalized to mean values for mock-infected mice within each bone type and measurement method group. Primary data are provided in Table S1 in the supplemental material. (A and B) Mean (± standard error of the mean) areal and volumetric BMDs (A) and BMD T-scores (B). (C and D) Representative 3D μCT models of trabecular bone from femoral metaphyses (C) and vertebrae (D). Scale bar, 200 μm. Additional representative 3D μCT models of cortical bone are presented in Fig. S2A. $n = 14$ to 15 mice per group. Statistics used included a two-way analysis of variance with the Holm-Sidak posttest. *, $P < 0.05$ versus mock controls within bone and measurement type; #, $P < 0.05$ for long bones versus vertebrae.

dimensional (3D) microarchitectural reconstructions from μCT. To distinguish between potential effects on trabecular and cortical bone, μCT analysis of cortical bone was performed in femora at the midshaft (composed mainly of cortical bone), whereas analysis of trabecular bone in femora was conducted at the distal metaphyses, where trabecular bone is more abundant (36). BMD values are expressed as percentages of the values for corresponding mock-infected animals (Fig. 3A).

To determine if changes in BMD in infected mice were clinically significant, we also calculated T-scores from the BMD values for vertebrae and femora. A T-score represents the number of standard deviations in the individual's BMD below the mean BMD of healthy young adults. T-scores 1 to 2.5 standard deviations lower than normal BMD are indicative of osteopenia, and T-scores more than 2.5 standard deviations lower than normal BMD correspond to osteoporosis (32). Means of individual T-scores were compared between *B. burgdorferi*-infected and mock-infected mice (Fig. 3B).

These experiments revealed that BMD of femoral trabecular bone was significantly lower in infected than in mock-infected mice (Fig. 3A). Trabecular BMD in vertebrae of infected animals was reduced but not significantly, and cortical BMD was not affected by *B. burgdorferi* infection (Fig. 3A). Examination of mean T-scores for bones from infected mice indicated that significant osteopenia was present in femora but not vertebrae (Fig. 3B). Representative reconstructed 3D models also showed visibly reduced bone volume and compactness from *B. burgdorferi* infection in the trabecular bone of femora, but the difference appeared less prominent in vertebral trabecular bone (Fig. 3C and D). Finally, to assess whether reductions in the BMD and T-scores were a function of increasing bacterial DNA burden, we calculated correlation coefficients for *flaB*:*nidogen* copy number ratios and areal and volumetric BMDs and T-scores in long bones and vertebrae (Table 1). All parameters were significantly negatively

TABLE 1 Correlation analyses of relationships between *B. burgdorferi* DNA burden and DXA and μCT parameters

Bone type and correlation statistics	Correlation[a] between bacterial DNA burden and:								
	aBMD	vBMD	T-score (aBMD)	T-score (vBMD)	BV/TV (μCT)	BS/BV (μCT)	Tb.N (μCT)	Tb.Pf (μCT)	Tb.Sp (μCT)
Long bones									
r (*P* value)	−0.50 (<0.05*)	−0.66 (<0.01*)	−0.51 (<0.01*)	−0.66 (<0.01*)	−0.66 (<0.01*)	0.61 (<0.01*)	−0.57 (<0.01*)	0.68 (<0.01*)	0.48 (<0.05*)
Vertebrae									
r (*P* value)	−0.12 (>0.05)	−0.079 (>0.05)	−0.049 (>0.05)	−0.079 (>0.05)	−0.13 (>0.05)	−0.018 (>0.05)	−0.15 (>0.05)	−0.019 (>0.05)	0.38 (>0.05)

[a]Asterisks indicate statistically significant correlations. Correlation analyses were performed by comparing DXA and μCT parameters to the mock background-corrected *flaB:nido* ratio for the same sample. Abbreviations: aBMD, areal bone mineral density; vBMD, volumetric bone mineral density; BV/TV, bone volume/tissue volume; BS/BV, bone surface/bone volume; Tb.N, trabecular number; Tb.Pf, trabecular pattern factor; Tb.Sp, trabecular separation.

correlated with bacterial DNA burden, i.e., BMD and T-scores decreased as *flaB:nidogen* copy numbers increased. We concluded that *B. burgdorferi* infection was associated with clinically significant bacterial DNA load-dependent osteopenia in long bones but not vertebrae and that bone loss was confined to trabecular bone.

Effects of *B. burgdorferi* infection on trabecular and cortical microarchitecture in long bones and vertebrae. To assess if trabecular bone microarchitecture deterioration was caused by infection, we measured the following parameters: BV/TV (the fraction of bone volume [BV] within total measured tissue volume [TV] of interest); BS/BV (the ratio of the bone surface [BS] to total bone volume [BV]), trabecular number (Tb.N, the average number of trabeculae per millimeter), trabecular separation (Tb.Sp, the mean distance between trabeculae), and the trabecular pattern factor (Tb.Pf, the intertrabecular connectivity, determined by assessing the relationship between convex and concave trabecular surfaces) (33). BV/TV, BS/BV, Tb.N, Tb.Sp, and Tb.Pf values were determined in three dimensions for the left femora and L5 vertebrae by using μCT. The same parameters, except Tb.Pf, were also measured in two dimensions in the proximal region of left tibiae and L3 vertebrae by histomorphometry performed in trichrome-stained bone sections. This permitted evaluation of bone structure by multiple methods, as well as comparison of effects of infection in different long bones.

μCT analyses of trabecular bone from distal metaphyses of femora showed that bone comprised a significantly smaller proportion of total measured tissue volume in infected mice than in mock-infected controls (Fig. 4A, BV/TV), and BV/TV ratios decreased as *B. burgdorferi* DNA burden increased (Table 1). Infection was also associated with significantly increased bone surface per bone volume ratios in the femora (Fig. 4B, BS/BV), which also increased with increasing bacterial DNA load (Table 1). Trabecular number (Tb.N) was significantly lower in femora of infected animals (Fig. 4C) and was negatively correlated with *B. burgdorferi* DNA burden (Table 1). Moreover, the trabecular pattern factor (Tb.Pf) parameter was greater in infected femora (Fig. 4D) and increased with bacterial DNA load (Table 1), indicating more poorly connected spongy lattices (33). A corresponding increase in trabecular separation (Tb.Sp) that was positively correlated with *flaB* copy number was observed in infected femora (Table 1; Fig. 4E). Histomorphometry analyses of trabecular bone from trichrome-stained sections of proximal tibiae also revealed significant reductions in BV/TV in infected mice (Fig. 4A). BS/BV (Fig. 4B) and Tb.Sp (Fig. 4E) values increased by a similar percentage in femora (μCT) and tibiae (histomorphometry) of infected animals, but the changes observed in tibiae were not significant, possibly due to inherently greater variations in histomorphometry sectioning and measurements. Tb.N did not differ in tibiae and femora of mock-infected and infected mice (Fig. 4C). Collectively, these analyses indicated that trabecular bone in the long bones of *B. burgdorferi*-infected mice was more porous and was composed of smaller, more poorly connected trabeculae, consistent with the observed osteopenia.

In contrast to the findings with long bones, neither μCT nor histomorphometry nor *flaB* copy number correlation analyses of vertebrae revealed significant infection-dependent changes in BV/TV, BS/BV, Tb.Sp, or Tb.Pf (Fig. 4A, B, and D; Table 1). Representative sections also showed that bone volume was reduced more dramatically by infection in tibiae than in vertebrae (Fig. 4F and G). Additionally, Tb.N was similar in
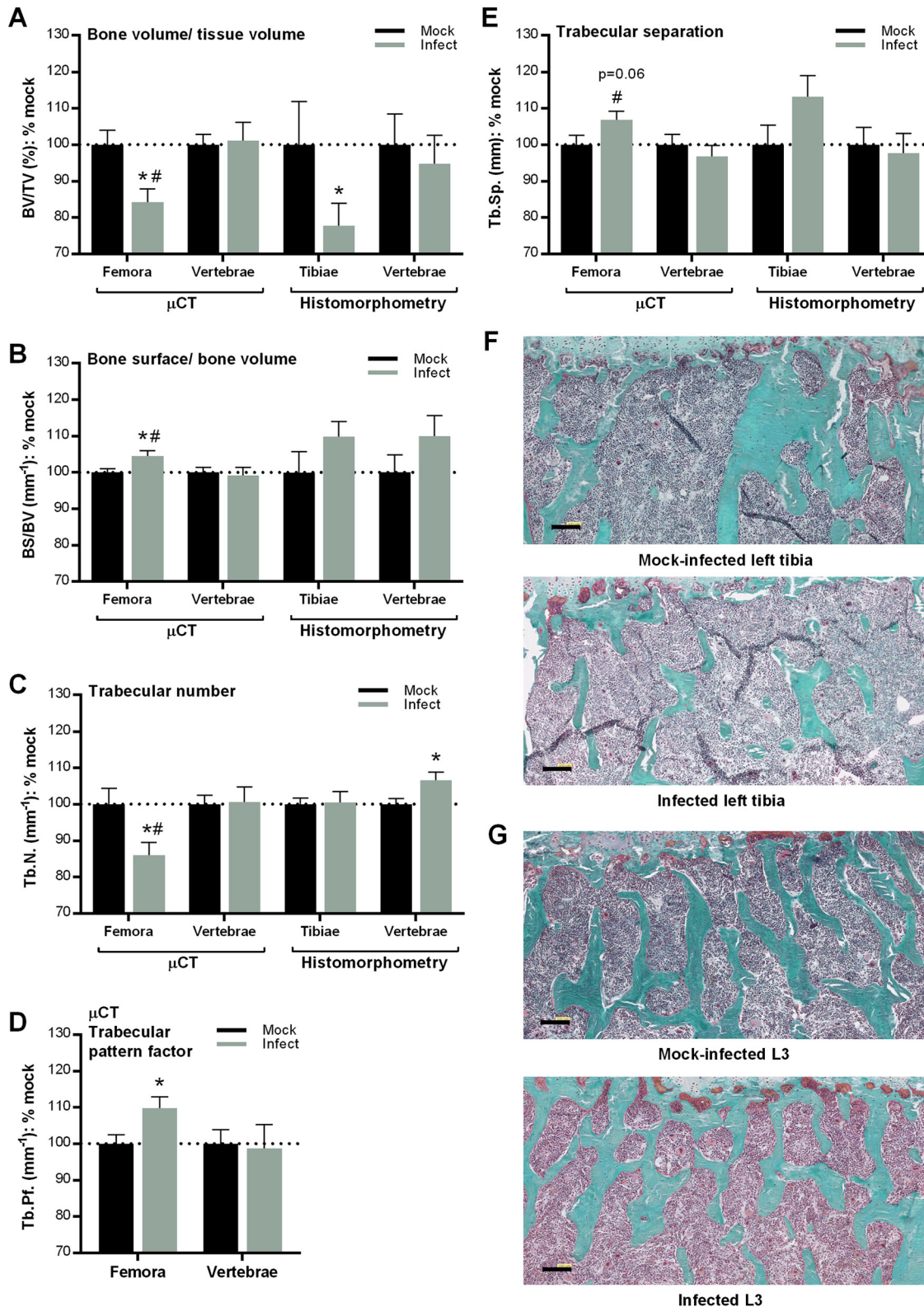
FIG 4 Effect of *B. burgdorferi* infection on trabecular bone microarchitecture. (A to E) Microarchitectural parameters of trabecular bone, measured by μCT (distal femoral metaphyses and L5 vertebrae) and histomorphometric analysis of trichrome-stained sections (proximal tibial metaphyses and L3 vertebrae). Shown are mean (± standard error of the mean) values normalized to means for mock-infected mice. Primary data are provided in Tables S1 and S2 in the supplemental material. $n = 14$ to 15 mice per group. Statistics used included a two-way analysis of variance with the Holm-Sidak posttest. *, $P < 0.05$ versus mock controls, within bone and measurement type; #, $P < 0.05$ for long bones versus vertebrae. (F and G) Representative sections from trichrome-stained left tibiae (F) and L3 vertebrae (G). Bar, 100 μm. Additional representative TRAP-stained sections are presented in Fig. S2B.

TABLE 2 Biomechanical properties of femoral midshafts, assessed by three-point bending

Biomechanical category and property	Value (mean ± SEM) for group[a]	
	Mock infected	Infected
Structural properties		
Peak load (N)	21.78 ± 0.68	22.15 ± 0.34
Failure displacement (mm)	0.13 ± 0.0036	0.14 ± 0.0031
Work to failure (mJ)	1.48 ± 0.077	1.58 ± 0.053
Stiffness (N/mm)	198.50 ± 4.72	193.10 ± 3.40
Mechanical properties		
Ultimate stress (MPa)	183.40 ± 5.23	191.20 ± 7.38
Failure strain (%)	1.94 ± 0.064	1.99 ± 0.056
Toughness (mJ/mm³)	168.70 ± 10.56	166.50 ± 8.07
Young's modulus (GPa)	11.16 ± 0.17	11.41 ± 0.23

[a]No significant differences were found between the mock and infected groups for any measured parameter (two-tailed unpaired t test; $P > 0.05$).

μCT-analyzed vertebrae from both experimental groups but was significantly greater in the vertebrae of infected than mock-infected mice when analysis was performed by histomorphometry (Fig. 4C). The discrepancy in these results suggests that the effect of infection on trabecular number was likely mild and was possibly less frequently observed in some vertebrae than others, likely due to a low *B. burgdorferi* DNA load in the vertebrae compared (Fig. 2). Together, these data showed that *B. burgdorferi* infection did not affect vertebral trabecular bone microarchitecture as strongly as it affected long bone microarchitecture, consistent with the results of BMD assays.

To assess the effects of *B. burgdorferi* infection on cortical bone microarchitecture, we measured cortical bone perimeter (B.Pm), thickness, cross-sectional area, and anteroposterior (AP) and mediolateral (ML) diameters in femoral midshafts via μCT. None of these properties differed significantly in infected versus mock-infected groups (see Table S1 in the supplemental material). Furthermore, three-point bending at the midshafts of the same femora revealed that infection did not affect cortical bone biomechanical properties (Table 2). Together with the results of BMD assays, these results implied that *B. burgdorferi* infection did not affect the structure or function of cortical bone.

Collectively, these data indicated that *B. burgdorferi* infection significantly disrupted the trabecular microarchitecture of long bones without affecting the vertebrae or cortical bone.

Bone loss in long bones of *B. burgdorferi*-infected mice is associated with reduced numbers of osteoblasts but does not affect osteoblast activity or osteoclast numbers. Healthy bone remodeling in response to stressors results from balance between bone-degrading activities of osteoclasts and the bone-building activities of osteoblasts (34). Increased osteoclastogenesis and osteoclast activity can result in increased number and size of osteoclasts at the bone surface, which lead to net bone resorption. This is frequently observed in bone loss due to local or systemic inflammation (8). In contrast, osteoblast apoptosis (i.e., decreased osteoblast numbers) and inhibition of osteoblast function (i.e., lower osteoid production, slower mineralization rate) are more prominent in bone loss associated with direct infection of bone (i.e., osteomyelitis) (9).

To determine whether osteopenia in trabecular regions of long bones in *B. burgdorferi*-infected mice was associated with changes in bone cell numbers, we measured the osteoclast number per bone surface (Oc.N/BS) in tartrate-resistant acid phosphatase (TRAP)-stained sections of right proximal tibial metaphyses and L4 vertebrae, and also osteoblast numbers per bone surface (Ob.N/BS) in trichrome-stained sections of the left proximal tibial metaphyses and L3 vertebrae (Fig. 5A and B). We also measured the ratio of total osteoclast surface to total bone surface (Oc.S/BS) and osteoid surface to bone surface (OS/BS) from the same sections (Fig. 5C and D).

Since *B. burgdorferi*-induced pathology in most tissues is primarily due to host inflammatory responses to these bacteria (3), we expected that bone loss in infected
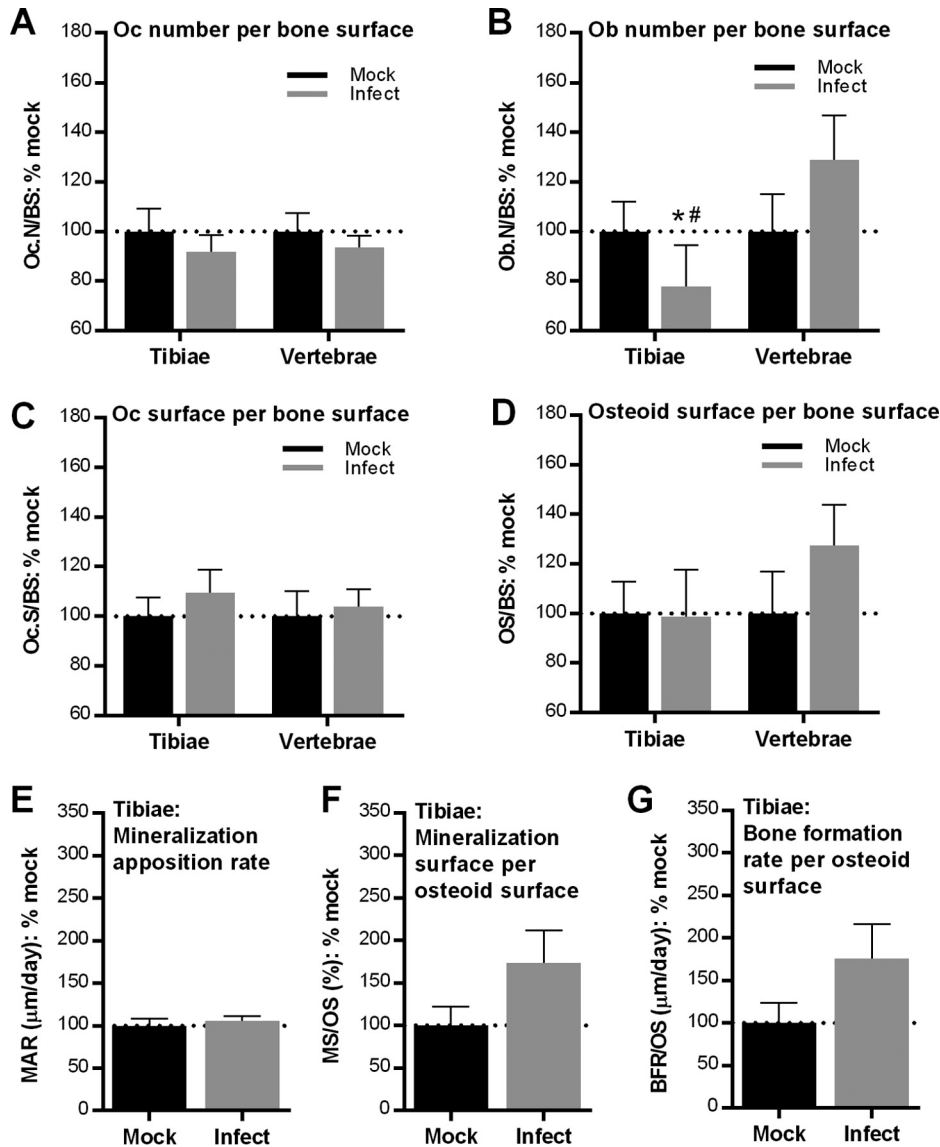
FIG 5 Effect of *B. burgdorferi* infection on cellular composition and activity in bone (A to D). Static histomorphometry analysis of numbers of osteoclasts (Oc) and osteoblasts (Ob) per bone surface (A and B) and osteoclast and osteoid surface per bone surface (C and D). Osteoclast parameters were measured in TRAP-stained sections of right proximal tibial metaphyses and L4 vertebrae. Osteoblast and osteoid parameters were measured in trichrome-stained sections of left proximal tibial metaphyses and L3 vertebrae. (E and G) Dynamic histomorphometry analysis of mineral apposition rate/day (E), mineralization surface/osteoid surface (F), and bone formation rate per osteoid surface (G) in left proximal tibial metaphyses, measured by imaging with fluorescent calcein green. For all groups, mean ($\pm$ standard error of the mean) values for parameters were normalized to the mean value for mock-infected mice. Primary data are provided in Table S2 in the supplemental material. Statistics used included a two-way analysis of variance with the Holm-Sidak posttest (A and B) and two-tailed unpaired *t* tests (C to E). *, $P < 0.05$ versus mock controls within bone and measurement type; #, $P < 0.05$ for long bones versus vertebrae.

mice would be accompanied by significant osteoclast-driven bone resorption. However, we found that osteoclast numbers (Fig. 5A) and coverage of bone surfaces (Fig. 5C) did not significantly increase in either the tibiae or vertebrae of infected mice. Instead, we observed that bone loss was accompanied by reduced osteoblast numbers at bone surfaces in tibiae (Fig. 5B), although reductions in osteoblast numbers did not appear to depend on bacterial DNA burden (Table S3). Osteoblast numbers in vertebrae were significantly greater than in tibiae (Fig. 5B), suggesting that differences in osteoblast numbers possibly contributed to differences in the bone loss phenotypes in these bones.

Despite reduced osteoblast numbers in the tibiae (Fig. 5B), osteoid production in bones of infected mice was not impaired (Fig. 5D). This implied that infection did not inhibit the activity of the osteoblasts present in bone. To further test this conclusion, rates of mineralized bone formation over time were examined via dynamic histomorphometry in calcein-labeled bone (Fig. 5E to G). Mineralization apposition rates (MARs) in infected and mock-infected animals were similar (Fig. 5E), as was the ratio of mineralization surface area to osteoid surface area (MS/OS) (Fig. 5F). Furthermore, infection did not reduce bone formation rate/osteoid surface ratios (BFR/OS) (Fig. 5G), implying that growth rates for mineralized bone were not affected when adjusted for osteoid volume. Thus, we concluded that although osteoblast numbers were reduced, osteoid production and mineralization were not affected by infection. Collectively, these data indicated that *B. burgdorferi* infection-dependent bone loss was associated with reductions in osteoblast numbers in long bones, but not with increased osteoclastogenesis, increased osteoclast activity, or impaired osteoblast activity.

DISCUSSION

In this study, we found that *B. burgdorferi* infection in mice is associated with infectious dose- and time-dependent reductions in ALP, a serum biomarker of bone formation in mice. Infection is also associated with *B. burgdorferi* DNA burden-dependent osteopenia and disrupted trabecular microarchitecture in long bones but not in vertebrae. These effects were not associated with increased osteoclast-dependent bone resorption, inhibition of osteoblast synthesis of osteoid cells, or bone mineralization. Instead, trabecular bone loss was associated with osteoblast number reductions in long bones but not in vertebrae. It is likely that differences in the effect of *B. burgdorferi* infection in long bones and vertebrae were due at least in part to differences in bacterial DNA burdens in these bones. Many bone loss parameters were significantly correlated with *flaB* copy number in long bones but not in vertebrae, suggesting that *B. burgdorferi* did not appear to colonize and/or persist as effectively in vertebral bone. However, other differences between long bones and vertebrae may have also contributed to differences in susceptibility to *B. burgdorferi* infection and infection outcomes, since long bones and vertebrae have been observed to be affected differently by systemic factors (e.g., rosiglitozone treatment) for reasons that remain unknown (30).

Although bone pain and bone involvement have been described in patients with Lyme disease (5, 12–18, 20, 21) and *B. burgdorferi* has been detected in human bone and bone marrow (10–13), the possibility that *B. burgdorferi* may infect and cause pathology in bone at sites other than articular surfaces has not been widely investigated. We found that *B. burgdorferi* infection in mice causes a level of osteopenia in the trabecular regions of long bones that would be considered a clinically significant finding in humans. However, structural and biomechanical properties of cortical bone were not affected by infection. It will be important to determine if conditions such as prolonged *B. burgdorferi* infection or infection in the context of preexisting osteopenia or osteoporosis would eventually result in a clinically symptomatic phenotype in cortical bone. It may also be useful to determine if *B. burgdorferi* infection in humans is associated with increased rates and severity of osteopenia and osteoporosis, and/or increased risk of fracture outcomes.

Bone loss results from an imbalance between the bone-resorbing activities of osteoclasts and bone-building functions of osteoblasts. Our data suggest that bone loss at 4 weeks postinfection was not primarily due to increased osteoclastogenesis or osteoclast activation, although it is possible that osteoclast-driven bone loss occurred earlier in infection. This is plausible, because tumor necrosis factor alpha (TNF-α), interleukin-1 (IL-1), IL-6, and IL-17, which are systemically upregulated in response to *B. burgdorferi* infection (35–38), are some of the major inflammatory cytokines that stimulate osteoclastogenesis and osteoclast activation (8, 39). TNF-α, IL-1, and IL-6 also suppress differentiation of osteoblasts (8), which is consistent with our observation that osteoblast numbers were reduced in bones which exhibited osteopenia. However,

regardless of whether increased osteoclast-dependent resorption was responsible for early bone loss in infection, data from the present study suggest that osteoblast deficiency makes important, long-lasting contributions to bone loss.

The major causes of osteoblast-related abnormalities in bone disease are loss or reduction of signals required for osteoblast differentiation (e.g., hormones or local regulatory proteins, such as bone morphogenetic proteins), differentiation of bone marrow mesenchymal stem cells into cells of nonosteoblastic lineage, premature osteoblast cell death, and inhibition of osteoblast activities (i.e., osteoid synthesis and mineralization) (40). We did not find that osteoid production or mineralization by the osteoblasts present in bones of infected mice were impaired, implying that osteoblast abnormalities occurred instead due to suppression of osteoblastogenesis or reduced osteoblast viability. It is unknown if *B. burgdorferi* infection affects mesenchymal stem cell differentiation or other major regulators of osteoblastogenesis, such as growth hormones, growth factors, estrogen, and parathyroid hormone (40). However, one of *B. burgdorferi*'s complement-regulating surface proteins, CRASP-1, is known to bind bone morphogenetic protein-2 (BMP-2) (41), a potent inducer of osteoblast differentiation (40). Treatment with vitamin D, another key regulator of osteoblastogenesis, has also been shown to reduce the severity of Lyme arthritis in mouse models (42). Additionally, direct or indirect bacterial induction of cell death in osteoblast lineage cells is a known important mediator of bone loss seen in osteomyelitis caused by other bacterial species (9). *B. burgdorferi* is known to induce cell death in a number of cell types, including glia, neurons, oligodendrocytes, lymphocytes, monocytes, and macrophages (43–48), but the effect of this bacterium on osteoblast biology and cell death have not yet been examined. These literature observations, together with our findings, warrant future investigations on the effect of *B. burgdorferi* infection on osteoblastogenesis and osteoblast viability.

In summary, this paper presents the first animal study directly demonstrating an effect of *B. burgdorferi* infection on bone tissue deterioration at sites other than articular surfaces involved in Lyme arthritis. Since these observations may have implications for our understanding of Lyme disease in humans, further investigation of the mechanisms underlying bone loss in response to *B. burgdorferi* infection is warranted.

MATERIALS AND METHODS

Ethics statements. All animal procedures were approved by the University of Toronto Animal Care Committee (protocol 20011501). Mice were housed in a biosafety level 2 room in groups of 2 to 4 per cage, with *ad libitum* access to food and water. Mice were anesthetized to a surgical plane of anesthesia by intraperitoneal injection of 200 mg/kg of body weight ketamine hydrochloride (Rogar/STB, Montréal, QC, Canada) and 10 mg/kg xylazine (MTC Pharmaceuticals, Cambridge, ON, Canada) before tissue harvesting and euthanasia.

Animal husbandry and dietary conditions. Upon arrival, 4-week-old male C3H/HeNCrl mice (Charles River, Montréal, QC, Canada) were fed standard chow (Teklad 2018 rodent chow; Harlan Laboratories, Mississauga, ON, Canada). At 12 weeks of age, mice were switched to a maintenance diet containing 0.6% calcium (Teklad 2014 rodent chow; Harlan Laboratories) until sacrifice.

B. burgdorferi cultivation and mouse infections. The *B. burgdorferi* strain used in this study was B31 5A4-derived GCB726 (49). As described elsewhere (50), this strain was cultivated to log phase in Barbour-Stoenner-Kelly II (BSK-II) medium before infection experiments. At 12 weeks of age, randomly assigned mice were inoculated subcutaneously at the dorsal lumbar midline with *B. burgdorferi* or BSK-II medium alone (mock infection). With the exception of the experiments presented in Fig. 1 and also Fig. S1 in the supplemental material, mice were infected with 10^4 *B. burgdorferi* for a period of 4 weeks. Each of these mice was also intraperitoneally injected with freshly prepared, 30 mg/kg 0.6% calcein green (Sigma-Aldrich Canada, Oakville, ON) at 9 and 2 days prior to sacrifice, to label newly formed bone.

Harvesting and preparation of sera and bones. Blood was collected by cardiac puncture from anesthetized mice before euthanasia by cervical dislocation, as described previously (50). Serum was harvested after overnight incubation at 4°C by centrifugation at 10,000 × *g* for 10 min.

The following bones were collected for all other analyses in this study: femora, tibiae, and L3 to L6 vertebrae. The left femora and L5 vertebral columns were cleaned of adherent soft tissue, wrapped in saline-soaked gauze, and stored at −20°C. These bones were thawed overnight at 4°C before DXA, μCT, and biomechanical analyses. Tibiae were excised and clipped at the midshaft into proximal and distal halves. Proximal metaphyses of the right tibiae and L4 vertebral columns were fixed immediately in 10% buffered formalin (Sigma) and decalcified in 14% EDTA (pH 7.4) at 4°C for 21 days, with solutions replaced every 2 days. These samples were then processed by the Toronto Centre for Phenogenomics (see the "Bone histomorphometry" section). Proximal metaphyses of the left tibiae and L3 vertebral columns were

fixed in 70% ethanol and stored at 4°C until submission to the Toronto Centre for Phenogenomics for processing (see details in the "Bone histomorphometry" section). Distal tibial halves and L6 vertebral bodies cleaned of adherent soft tissue were stored at −80°C until DNA extraction for qPCR analysis. All extractions were performed using bone distal from joints to ensure that any bacterial DNA detected was not joint derived.

Serum ALP activity assays. Serum ALP activity was measured in technical duplicates using a colorimetric ALP assay kit (Abcam, Cambridge, UK) following the manufacturer's instructions.

DNA extraction and qPCR measurement of *B. burgdorferi* DNA copy number. For DNA extraction, bones were thoroughly cleaned of peripheral soft tissue, and bone marrow was removed by flushing with a syringe. Cleaned, rinsed bones were then pulverized with a mortar and pestle on dry ice. DNA was extracted from pulverized bone using Qiagen DNeasy tissue extraction kits (Toronto, ON, Canada) as per the manufacturer's instruction. Concentration of extracted DNA were measured using a Nanodrop spectrophotometer (Thermo Fisher Scientific, Waltham, MA, USA). Measurement of numbers of copies of *B. burgdorferi flaB* DNA by qPCR was performed in technical sextuplicates as described previously (50), using triplicate logarithmic dilutions (10^1 to 10^6 copies) of plasmid pTM222 (which contained a copy of the *flaB* DNA sequence) as a standard curve. The mean of technical replicates was used for subsequent analyses, and findings were expressed as the ratio per 1,000 copies of mouse *nidogen* DNA measured by qPCR from the same sample. For each bone type, the median *flaB:nidogen* ratio from mock-infected mice was subtracted from *flaB:nidogen* ratios from infected and mock-infected animals.

qPCR for mouse *nidogen* was performed with logarithmic dilutions of plasmid standard pTM221 containing the *nidogen* target amplification sequence (standard range, 1 to 10^8 copies/reaction mixture). pTM221 (*Escherichia coli* strain GCE1844) was cloned by PCR amplifying the *nidogen* target sequence from mouse genomic DNA with primers nido.F (5'-CGAGCCACAGAATACCATCC-3') and nido.R (5'-GGA CATACTCTGCTGCCATC-3') into the pJET1.2/Blunt cloning vector using the CloneJet PCR cloning kit (Thermo-Fisher Scientific), followed by sequencing of the insert. qPCR was performed as described for *flaB* (50), using primers nido.F and nido.R (51). qPCR conditions were 95°C for 5 min, followed by 50 cycles of 98°C for 5.75 s, 60°C for 2.75 s, and 86°C for 5 s, and then melt curve analysis ranging from 60°C to 95°C. Average *nidogen* copy numbers obtained from triplicate reaction mixtures were used for normalization of *flaB* copy numbers.

BMD and morphometry measurements. Measurement of areal bone mineral density (aBMD, in grams per centimeter squared) in left femora and L5 vertebral bodies was performed by DXA using a PIXImus mouse bone densitometer (GE Medical Systems, Madison, WI). Measurements of volumetric bone mineral density (vBMD, in grams per cubic centimeter) and morphometry from trabecular and cortical bones of left femora, as well as from L5 vertebral bodies, were performed after DXA analysis by μCT, using a SkyScan 1174 μCT scanner (Bruker microCT, Kontich, Belgium). Images were acquired at 50 kV and 800 μA, and a 0.25-mm aluminum filter was applied for noise removal. Two hydroxyapatite (HA) phantoms were scanned and used to calculate vBMD. Structural indices were computed using the SkyScan CT Analyzer software. Following image acquisition, three-dimensional reconstruction was performed to calculate bone microarchitecture parameters. Morphometry measurements were performed with global thresholding to exclude soft tissue (trabecular bone, 0.9 g HA/cm³; gray value, 65; cortical bone, 1.1 g HA/cm³; gray value, 100).

For trabecular bone analyses, distal femoral metaphyses and L5 vertebrae were scanned at a voxel size of 6.1 μm³. The volume of interest (VOI) for femora consisted of a 400-slice (2.4-mm) section extending 50 slices (0.3 mm) from the first cartilage bridge of femur metaphyses. The VOI for L5 was between the growth plates, with a 50-slice (0.3-mm) offset from each. For cortical bone analyses, femoral middiaphyses were scanned at 11.6 μm³. The VOI for cortical bone was a 100-slice (1.16-mm) section at the middiaphysis.

Biomechanical testing. After μCT analysis, biomechanical properties of the left femorae were assessed by three-point bending at the midshaft, using an ElectroPuls E1000 machine (Instron Corp., Canton, MA, USA) with a 100-N load cell. Femora were placed anteriorly face up on two supports, 7 mm apart. A pretest of 10 cycles (maximum, 5-N load; minimum, 2-N load) was applied to each femur. A destructive load was then vertically applied to the midshaft at 2.0 mm/min until failure. Load deformation curves derived from biomechanical testing were generated using the accompanying Bluehill 3 software (Instron). Parameters were calculated using geometry measurements for cortical bone from the μCT data.

Bone histomorphometry. Tartrate-resistant acid phosphatase (TRAP) staining for identification of osteoclasts was performed on 5-μm-thick sections cut from formalin-fixed, decalcified right tibiae and L4 vertebrae embedded in paraffin. Ethanol-fixed, undecalcified left tibiae and L3 vertebrae were embedded in methylmethacrylate, sectioned, and stained with Goldner's trichrome (4-μm-thick sections) or left unstained for measurement of calcein fluorescence (7-μm-thick sections). All histology services were performed by the Toronto Phenogenomics Centre.

Static and dynamic histomorphometry analyses of TRAP-stained, trichrome-stained, and calcein green-labeled sections were performed manually using BioQuantOsteo v11.2.6. All histomorphometric measurements were performed and analyzed following guidelines from the American Society of Bone and Mineral Research (52).

Statistical analyses. Statistical analyses were performed in Prism v.6.0 (GraphPad Software, La Jolla, CA, USA). Specific tests used for analyses are indicated in the figure legends and table footnotes. Pearson correlation analyses were performed for log-transformed *flaB* copy numbers per 1,000 *nidogen* copies and various bone parameters from each mouse. Data were considered statistically significant at a confidence level of 95% ($P < 0.05$).

REFERENCES

1. Mead PS. 2015. Epidemiology of Lyme disease. Infect Dis Clin North Am 29:187–210. https://doi.org/10.1016/j.idc.2015.02.010.
2. Stanek G, Wormser GP, Gray J, Strle F. 2012. Lyme borreliosis. Lancet 379:461–473. https://doi.org/10.1016/S0140-6736(11)60103-7.
3. Weis J, Bockenstedt L. 2010. Host response, p 413–442. In Radolf JD, Samuels DS (ed), Borrelia: molecular biology, host interaction, and pathogenesis. Caister Academic Press, Norfolk, United Kingdom.
4. Shapiro ED. 2014.Clinical practice. Lyme disease. N Engl J Med 371: 1724–1731. https://doi.org/10.1056/NEJMcp1314325.
5. Steere AC, Schoen RT, Taylor E. 1987. The clinical evolution of Lyme arthritis. Ann Intern Med 107:725–731. https://doi.org/10.7326/0003-4819-107-5-725.
6. Park K-H, Lee MS, Hong IK, Sung J-Y, Choi S-H, Park SO, Shin MJ, Chung HW, Lee SH. 2014. Bone involvement in secondary syphilis: a case report and systematic review of the literature. Sex Transm Dis 41:532–537. https://doi.org/10.1097/OLQ.0000000000000164.
7. Silva N, Abusleme L, Bravo D, Dutzan N, Garcia-Sesnich J, Vernal R, Hernández M, Gamonal J. 2015. Host response mechanisms in periodontal diseases. J Appl Oral Sci Rev 23:329–355. https://doi.org/10.1590/1678-775720140259.
8. Redlich K, Smolen JS. 2012. Inflammatory bone loss: pathogenesis and therapeutic intervention. Nat Rev Drug Discov 11:234–250. https://doi.org/10.1038/nrd3669.
9. Marriott I. 2013. Apoptosis-associated uncoupling of bone formation and resorption in osteomyelitis. Front Cell Infect Microbiol 3:101. https://doi.org/10.3389/fcimb.2013.00101.
10. Hovius KE, Rijpkema SG, Westers P, van der Zeijst BA, van Asten FJ, Houwers DJ. 1999. A serological study of cohorts of young dogs, naturally exposed to Ixodes ricinus ticks, indicates seasonal reinfection by Borrelia burgdorferi sensu lato. Vet Q 21:16–20. https://doi.org/10.1080/01652176.1999.9694985.
11. Keller A, Graefen A, Ball M, Matzas M, Boisguerin V, Maixner F, Leidinger P, Backes C, Khairat R, Forster M, Stade B, Franke A, Mayer J, Spangler J, McLaughlin S, Shah M, Lee C, Harkins TT, Sartori A, Moreno-Estrada A, Henn B, Sikora M, Semino O, Chiaroni J, Rootsi S, Myres NM, Cabrera VM, Underhill PA, Bustamante CD, Vigl EE, Samadelli M, Cipollini G, Haas J, Katus H, O'Connor BD, Carlson MRJ, Meder B, Blin N, Meese E, Pusch CM, Zink A. 2012. New insights into the Tyrolean Iceman's origin and phenotype as inferred by whole-genome sequencing. Nat Commun 3:698. https://doi.org/10.1038/ncomms1701.
12. Oksi J, Mertsola J, Reunanen M, Marjamäki M, Viljanen MK. 1994. Sub-

acute multiple-site osteomyelitis caused by Borrelia burgdorferi. Clin Infect Dis 19:891–896. https://doi.org/10.1093/clinids/19.5.891.
13. Schlesinger PA, Duray PH, Burke BA, Steere AC, Stillman MT. 1985. Maternal-fetal transmission of the Lyme disease spirochete, Borrelia burgdorferi. Ann Intern Med 103:67–68. https://doi.org/10.7326/0003-4819-103-1-67.
14. Houtman PM, Tazelaar DJ. 1999. Joint and bone involvement in Dutch patients with Lyme borreliosis presenting with acrodermatitis chronica atrophicans. Neth J Med 54:5–9. https://doi.org/10.1016/S0300-2977(98)00093-X.
15. Hovmark A, Asbrink E, Olsson I. 1986. Joint and bone involvement in Swedish patients with Ixodes ricinus-borne Borrelia infection. Zentralbl Bakteriol Mikrobiol Hyg A 263:275–284.
16. Kvasnicka HM, Thiele J, Ahmadi T. 2003. Bone marrow manifestation of Lyme disease (Lyme borreliosis). Br J Haematol 120:723. https://doi.org/10.1046/j.1365-2141.2003.04084.x.
17. Lawson JP, Rahn DW. 1992. Lyme disease and radiologic findings in Lyme arthritis. AJR Am J Roentgenol 158:1065–1069. https://doi.org/10.2214/ajr.158.5.1566669.
18. Lawson JP, Steere AC. 1985. Lyme arthritis: radiologic findings. Radiology 154:37–43. https://doi.org/10.1148/radiology.154.1.3964949.
19. Munson E, Nardelli DT, Du Chateau BK, Callister SM, Schell RF. 2012. Hamster and murine models of severe destructive Lyme arthritis. Clin Dev Immunol 2012:504215.
20. Schmitz G, Vanhoenacker FM, Gielen J, De Schepper AM, Parizel PM. 2004. Unusual musculoskeletal manifestations of Lyme disease. JBR-BTR 87:224–228.
21. Steere AC. 1995. Musculoskeletal manifestations of Lyme disease. Am J Med 98:44S–48S. https://doi.org/10.1016/S0002-9343(99)80043-6.
22. Millán JL. 2006. Alkaline phosphatases: structure, substrate specificity and functional relatedness to other members of a large superfamily of enzymes. Purinergic Signal 2:335–341. https://doi.org/10.1007/s11302-005-5435-6.
23. Millán JL, Whyte MP. 2016. Alkaline phosphatase and hypophosphatasia. Calcif Tissue Int 98:398–416. https://doi.org/10.1007/s00223-015-0079-1.
24. Linder CH, Englund UH, Narikawa S, Millán JL, Magnussen P. 2013. Isozyme profile and tissue-origin of alkaline phosphatases in mouse serum. Bone 53:399–408. https://doi.org/10.1016/j.bone.2012.12.048.
25. Ferreira A, Alho I, Casimiro S, Costa L. 2015. Bone remodeling markers and bone metastases: from cancer research to clinical implications. Bonekey Rep 4:668. https://doi.org/10.1038/bonekey.2015.35.

26. Barthold SW, Cadavid D, Philipp MT. 2010. Animal models of borreliosis, p 359–411. In Radolf JD, Samuels DS (ed), Borrelia: molecular biology, host interaction, and pathogenesis. Caister Academic Press, Norfolk, United Kingdom.

27. Barthold SW, Beck DS, Hansen GM, Terwilliger GA, Moody KD. 1990. Lyme borreliosis in selected strains and ages of laboratory mice. J Infect Dis 162:133–138. https://doi.org/10.1093/infdis/162.1.133.

28. Willingham MD, Brodt MD, Lee KL, Stephens AL, Ye J, Silva MJ. 2010. Age-related changes in bone structure and strength in female and male BALB/c mice. Calcif Tissue Int 86:470–483. https://doi.org/10.1007/s00223-010-9359-y.

29. Buie HR, Moore CP, Boyd SK. 2008. Postpubertal architectural developmental patterns differ between the L3 vertebra and proximal tibia in three inbred strains of mice. J Bone Miner Res 23:2048–2059. https://doi.org/10.1359/jbmr.080808.

30. Viberti G, Kahn SE, Greene DA, Herman WH, Zinman B, Holman RR, Haffner SM, Levy D, Lachin JM, Berry RA, Heise MA, Jones NP, Freed MI. 2002. A diabetes outcome progression trial (ADOPT): an international multicenter study of the comparative efficacy of rosiglitazone, glyburide, and metformin in recently diagnosed type 2 diabetes. Diabetes Care 25:1737–1743. https://doi.org/10.2337/diacare.25.10.1737.

31. Miller JC, Ma Y, Bian J, Sheehan KCF, Zachary JF, Weis JH, Schreiber RD, Weis JJ. 2008. A critical role for type I IFN in arthritis development following Borrelia burgdorferi infection of mice. J Immunol 181: 8492–8503. https://doi.org/10.4049/jimmunol.181.12.8492.

32. Kanis JA, Glüer CC. 2000. An update on the diagnosis and assessment of osteoporosis with densitometry. Committee of Scientific Advisors, International Osteoporosis Foundation. Osteoporos Int 11:192–202. https://doi.org/10.1007/s001980050281.

33. Hahn M, Vogel M, Pompesius-Kempa M, Delling G. 1992. Trabecular bone pattern factor: a new parameter for simple quantification of bone microarchitecture. Bone 13:327–330. https://doi.org/10.1016/8756-3282(92)90078-B.

34. Clarke B. 2008. Normal bone anatomy and physiology. Clin J Am Soc Nephrol 3(Suppl 3):S131–S139. https://doi.org/10.2215/CJN.04151206.

35. Benhnia MR, Wroblewski D, Akhtar MN, Patel RA, Lavezzi W, Gangloff SC, Goyert SM, Caimano MJ, Radolf JD, Sellati TJ. 2005. Signaling through CD14 attenuates the inflammatory response to Borrelia burgdorferi, the agent of Lyme disease. J Immunol 174:1539–1548. https://doi.org/10.4049/jimmunol.174.3.1539.

36. Isogai E, Isogai H, Kimura K, Hayashi S, Kubota T, Nishikawa T, Nakane A, Fujii N. 1996. Cytokines in the serum and brain in mice infected with distinct species of Lyme disease Borrelia. Microb Pathog 21:413–419. https://doi.org/10.1006/mpat.1996.0072.

37. Zlotnikov N, Javid A, Ahmed M, Eshghi A, Tang TT, Arya A, Bansal A, Matar F, Parikh M, Ebady R, Koh A, Gupta N, Song P, Zhang Y, Newbigging S, Wormser GP, Schwartz I, Inman R, Glogauer M, Moriarty TJ. 29 October 2016. Infection with the Lyme disease pathogen suppresses innate immunity in mice with diet-induced obesity. Cell Microbiol https://doi.org/10.1111/cmi.12689.

38. Lasky CE, Jamison KE, Sidelinger DR, Pratt CL, Zhang G, Brown CR. 2015. Infection of interleukin 17 receptor A-deficient C3H mice with Borrelia burgdorferi does not affect their development of Lyme arthritis and carditis. Infect Immun 83:2882–2888. https://doi.org/10.1128/IAI.00533-15.

39. Yago T, Nanke Y, Ichikawa N, Kobashigawa T, Mogi M, Kamatani N, Kotake S. 2009. IL-17 induces osteoclastogenesis from human monocytes alone in the absence of osteoblasts, which is potently inhibited by anti-TNF-alpha antibody: a novel mechanism of osteoclastogenesis by IL-17. J Cell Biochem 108:947–955. https://doi.org/10.1002/jcb.22326.

40. Marie PJ. 2015. Osteoblast dysfunctions in bone diseases: from cellular and molecular mechanisms to therapeutic strategies. Cell Mol Life Sci 72:1347–1361. https://doi.org/10.1007/s00018-014-1801-2.

41. Hallstrom T, Haupt K, Kraiczy P, Hortschansky P, Wallich R, Skerka C, Zipfel PF. 2010. Complement regulator-acquiring surface protein 1 of Borrelia burgdorferi binds to human bone morphogenic protein 2, several extracellular matrix proteins, and plasminogen. J Infect Dis 202: 490–498. https://doi.org/10.1086/653825.

42. Cantorna MT, Hayes CE, DeLuca HF. 1998. 1,25-Dihydroxycholecalciferol inhibits the progression of arthritis in murine models of human arthritis. J Nutr 128:68–72.

43. Buffen K, Oosting M, Mennens S, Anand PK, Plantinga TS, Sturm P, van de Veerdonk FL, van der Meer JWM, Xavier RJ, Kanneganti T-D, Netea MG, Joosten LAB. 2013. Autophagy modulates Borrelia burgdorferi-induced production of interleukin-1β (IL-1β). J Biol Chem 288: 8658–8666. https://doi.org/10.1074/jbc.M112.412841.

44. Cruz AR, Moore MW, La Vake CJ, Eggers CH, Salazar JC, Radolf JD. 2008. Phagocytosis of Borrelia burgdorferi, the Lyme disease spirochete, potentiates innate immune activation and induces apoptosis in human monocytes. Infect Immun 76:56–70. https://doi.org/10.1128/IAI.01039-07.

45. Glickstein LJ, Coburn JL. 2006. Short report: association of macrophage inflammatory response and cell death after in vitro Borrelia burgdorferi infection with arthritis resistance. Am J Trop Med Hyg 75:964–967.

46. Perticarari S, Presani G, Prodan M, Granzotto M, Murgia R, Cinco M. 2003. Lymphocyte apoptosis co-cultured with Borrelia burgdorferi. Microb Pathog 35:139–145. https://doi.org/10.1016/S0882-4010(03)00096-2.

47. Ramesh G, Borda JT, Dufour J, Kaushal D, Ramamoorthy R, Lackner AA, Philipp MT. 2008. Interaction of the Lyme disease spirochete Borrelia burgdorferi with brain parenchyma elicits inflammatory mediators from glial cells as well as glial and neuronal apoptosis. Am J Pathol 173: 1415–1427. https://doi.org/10.2353/ajpath.2008.080483.

48. Thai PT, Collins CC, Fortner KA, Koenig A, Hayes SM, Budd RC. 2011. Increased caspase activity primes human Lyme arthritis synovial γδ T cells for proliferation and death. Hum Immunol 72:1168–1175. https://doi.org/10.1016/j.humimm.2011.08.019.

49. Moriarty TJ, Norman MU, Colarusso P, Bankhead T, Kubes P, Chaconas G. 2008. Real-time high resolution 3D imaging of the Lyme disease spirochete adhering to and escaping from the vasculature of a living host. PLoS Pathog 4:e1000090. https://doi.org/10.1371/journal.ppat.1000090.

50. Javid A, Zlotnikov N, Pĕtrošová H, Tang TT, Zhang Y, Bansal AK, Ebady R, Parikh M, Ahmed M, Sun C, Newbigging S, Kim YR, Santana Sosa M, Glogauer M, Moriarty TJ. 2016. Hyperglycemia impairs neutrophil-mediated bacterial clearance in mice infected with the Lyme disease pathogen. PLoS One 11:e0158019. https://doi.org/10.1371/journal.pone.0158019.

51. Morrison TB, Ma Y, Weis JH, Weis JJ. 1999. Rapid and sensitive quantification of Borrelia burgdorferi-infected mouse tissues by continuous fluorescent monitoring of PCR. J Clin Microbiol 37:987–992.

52. Dempster DW, Compston JE, Drezner MK, Glorieux FH, Kanis JA, Malluche H, Meunier PJ, Ott SM, Recker RR, Parfitt AM. 2013. Standardized nomenclature, symbols, and units for bone histomorphometry: a 2012 update of the report of the ASBMR Histomorphometry Nomenclature Committee. J Bone Miner Res 28:2–17. https://doi.org/10.1002/jbmr.1805.